Principal Interaction Patterns in Baroclinic Wave Life Cycles

U. ACHATZ, G. SCHMITZ, AND K.-M. GREISIGER

Institut für Atmosphärenphysik an der Universität Rostock, Kühlungsborn, Germany

(Manuscript received 3 July 1994, in final form 9 January 1995)

ABSTRACT

A principal interaction pattern (PIP) analysis aims at finding a limited number of structures in seemingly very complicated physical scenarios that are time independent up to their amplitudes and phases. These vary according to nonlinear equations determining the interaction between the different structures. By minimizing a suitably chosen error function, calculated by comparing a PIP model with observed or synthetic datasets, both the structures and their interaction coefficients are determined simultaneously. This might therefore be a useful tool for identifying basic structures and processes underlying baroclinic wave life cycles.

As a first step in this direction, an accordingly devised PIP model has been applied to a synthetic dataset obtained by numerically integrating the tendency equations of a very simple spherical and quasigeostrophic two-layer model incorporating surface drag and thermal damping. For fairly typical dissipative parameters, a PIP analysis identifies three basic structures that give a good description of the complete dynamics. The shape of these patterns and their interaction coefficients seem to be controlled by the diabatic parameters of the two-layer model. The initial conditions of an examined time series have virtually no influence. The role of the three PIPs in the baroclinic life cycle is discussed. An analysis of their interplay with each other and the zonal wind indicates that dissipation and forcing of the eddies themselves is an important factor in the maintenance of multiple baroclinic wave life cycles. Comparative analyses of cases with stronger and weaker dissipation indicate that the number of dynamically relevant patterns decreases with increasing dissipation, so that PIPs appear to be a valuable tool for the analysis of sufficiently dissipative systems.

1. Introduction

Starting with the classical work of Charney (1947) and Eady (1949), baroclinic instability has attracted broad interest as a tool for interpreting cyclone development. With its linear dynamics being mostly understood, the nonlinear dynamics of the problem has increasingly become the central field of research. A whole hierarchy of model types has been used for this purpose. Analytical studies (e.g., Pedlosky 1970) had to be limited to relatively simplified situations, such as very weak instability in a quasigeostrophic two-layer model on a β-plane. The case of strong instability in such models has been studied by numerical methods (e.g., Mak 1985; Feldstein and Held 1989). Meanwhile similarity with the real atmospheric situation had decisively been improved in simulations of the nonlinear development of baroclinic waves on a sphere using the primitive equations (Gall 1976; Simmons and Hoskins 1978; Frederiksen 1981). By these and later examinations following the same line (e.g., Young and Houben 1989; Branscome et al. 1989; Barnes and Young 1992; Thorncroft et al. 1993), it has been demonstrated that baroclinic waves undergo a clearly defined life cycle. Provided the basic zonal flow has sufficiently strong meridional shear, the baroclinic growth phase is followed by a mainly barotropic decay phase. In the presence of heating and surface friction, wave and basic zonal flow are prevented from finding an equilibrium, and several life cycles follow each other in a multiple fashion. Especially in the Northern Hemisphere, baroclinic waves appear often more as patterns of limited extent, like wave packets, than equally distributed along a latitude circle, as assumed in the work mentioned above. Wave packet dynamics and the associated downstream baroclinic development due to convergence and divergence of geopotential fluxes has therefore been the subject of several recent studies (e.g., Chang 1993; Orlanski and Chang 1993; Lee and Held 1993). Nevertheless, it has been possible to identify life cycle behavior in atmospheric observations (Randel and Stanford 1985a,b; Randel 1990), so that it can still be seen as an important corner stone for atmospheric cyclone behavior.

By the use of statistical methods, Schnur et al. (1993) have recently found characteristic patterns in observed Northern and Southern Hemispheric data

Corresponding author address: Dr. Ulrich Achatz, Institut für Atmosphärenphysik an der Universität Rostock, Schloßstraße 4-6, 18221 Kühlungsborn, Germany.

© 1995 American Meteorological Society

that are quite similar to baroclinic waves in the different phases of a life cycle. This has been motivation to examine the possibility of searching for such characteristic patterns in observed or model data on the basis of a dynamical approach. A principal interaction pattern (PIP) analysis as outlined by Hasselmann (1988) could possibly be a rather useful tool for this purpose. It aims at finding a limited number of structures in the seemingly very complicated dynamics that are time independent up to their amplitudes and phases. These vary according to nonlinear equations, determining the interaction between the different structures. By minimizing a suitably chosen error function, both these structures and their interaction coefficients are determined simultaneously. This work presents a first step toward using PIP models to study the different phases underlying baroclinic wave life cycles. For a start we examine this question using a synthetic dataset, which is obtained with a two-layer model.

In section 2 we will summarize the essentials of the two-layer model used. Section 3 presents the PIP model applied to the data. In section 4 we present the results of our PIP decomposition of these data for typical diabatic parameters. Baroclinic wave development will be discussed within the framework of the PIPs thus obtained. The work will be summarized in section 5.

2. The two-layer model

The data used in this work for a PIP analysis were obtained by numerical integration of the equations of a very simple two-layer model. Nevertheless, as will be seen later, it has sufficient similarity to the real atmosphere so as to be able to reproduce the main features of baroclinic wave life cycles. Starting with the quasigeostrophic version of the spherical two-layer model as formulated by Lorenz (1960), surface friction and Newtonian cooling are included. Furthermore, we have incorporated forcing terms that make a chosen zonal wind configuration a stationary solution of the system. To numerically stabilize the integrations, weak horizontal diffusion is also needed. Static stability is assumed to be a constant. The most drastic simplification is that the Coriolis parameter is replaced by a latitude-independent value in the thermal wind equation as well as in the term describing vertical advection [B-model; e.g., Baines and Frederiksen (1978)]. Thus we finally end up with two equations giving the necessary time derivatives:

$$\frac{\partial}{\partial t}\nabla^2\psi = -J(\psi, \nabla^2\psi) - J(\tau, \nabla^2\tau) - 2\frac{\partial\psi}{\partial\lambda} + k_s\nabla^2(\tau - \psi) + F_\psi - \kappa\nabla^2(\nabla^2(\nabla^2\psi)) \quad (1)$$

$$\frac{\partial}{\partial t}(\nabla^2 - r^2)\tau = -J[\psi, (\nabla^2 - r^2)\tau] - J(\tau, \nabla^2\psi) - 2\frac{\partial\tau}{\partial\lambda} - k_s\nabla^2(\tau - \psi) - h_N r^2(\tau_f - \tau) - \kappa(\nabla^2 - r^2)[\nabla^2(\nabla^2\tau)]. \quad (2)$$

By $\psi = (\phi_3 + \phi_1)/2$ and $\tau = (\phi_3 - \phi_1)/2$, barotropic and baroclinic streamfunctions are denoted, where ϕ_3 and ϕ_1 are the upper- and lower-layer streamfunctions; J is the Jacobian operator; k_s and h_N are Ekman surface friction and Newtonian cooling, respectively; F_ψ denotes zonal mean vorticity forcing; τ_f a forced zonal shear corresponding to the temperature distribution forced by Newtonian cooling; and κ is the horizontal diffusion applied to the equations. The parameter $r = 2\sin\varphi_0/\bar{\sigma}^{1/2}$ contains the latitude φ_0 chosen for the evaluation of the Coriolis parameter and the static stability $\bar{\sigma}$. The equations are nondimensionalized using a_0, $1/\Omega$, and $(a_0^2\Omega^2)/(c_p b)$ as length, time, and potential temperature scale, respectively. Here a_0 is the radius of earth, Ω its angular velocity, c_p the heat capacity of air at constant pressure, and $b = 0.124$. For a derivation of (1) and (2) see appendix A.

Because the quasigeostrophic approximation is invalid near the equator and variation of the Coriolis force with latitude is incompletely described by the model, only scenarios that are equatorially symmetric were considered; φ_0 was chosen to be 45°N. At least in middle latitudes the error made by the model should not be too dramatic. In the cases presented here we have used a static stability $\bar{\sigma} = 0.01$, corresponding to a temperature difference between the layers of 34.5 K. The horizontal diffusion used was $\kappa = 3 \times 10^{-6} a^4/d$, which is about as small as possible to prevent the adiabatic limit of the baroclinic wave life cycles examined here from eventually piling up energy at small scales.

For the determination of the synthetic dataset, all variables are represented by a truncated expansion in terms of spherical harmonics. Horizontal resolution comprises a rhomboidal spectral truncation at zonal and meridional wavenumber 15. An explicit time scheme using a variable-order, variable-step Adams method was applied as the integration scheme for the spectral equations.

3. Principal interaction patterns

a. General method

The general idea of a PIP model is the following (Hasselmann 1988): Let us assume that we have a dynamical system that can be described at any moment by a complex-state vector $\Phi(t)$. Its time development shall be given by a set of first-order differential equations

$$\frac{d}{dt}\Phi = \mathbf{F}(\Phi, t), \tag{3}$$

where $\mathbf{F}$ may depend nonlinearly on Φ. For such a system, a PIP analysis tries to find a limited number of patterns $\mathbf{p}_\nu$ that in combination give an optimal representation of the complete-state vector at any time such that the residual error

$$\rho(t) = \Phi(t) - \sum_\nu a_\nu(t)\mathbf{p}_\nu \tag{4}$$

becomes as small as possible. The only time dependence is in the $a_\nu(t)$. Assuming the patterns $\mathbf{p}_\nu$ to be known, their coefficients can be determined by minimization of the residual error to be

$$a_\nu = \sum_\mu (N^{-1})_{\nu\mu} \sum_i \overline{p_{i\mu}}\Phi_i, \tag{5}$$

where i is the index of the state space spanned by the system and the matrix N is given by

$$N_{\nu\mu} = \sum_i \overline{p_{i\nu}}p_{i\mu}. \tag{6}$$

The overbar denotes complex conjugation. The dynamical aspect of the method enters with a second step, which makes PIPs so interesting for the reduction of complex dynamical systems. The evolution of the PIP coefficients is postulated to follow a set of nonlinear equations

$$\frac{da_\nu}{dt} = G_\nu(\mathbf{a}, \alpha_1, \cdots, \alpha_p), \tag{7}$$

with a small number of parameters α_q. In contrast to Hasselmann (1988), we will assume that some of these might also be connected to the patterns by some boundary conditions. To determine both parameters and patterns, a minimization of the error

$$\epsilon(\alpha_1, \cdots, \alpha_q, \mathbf{p}_1, \cdots, \mathbf{p}_M) = \sum_t |\dot{\Phi} - \dot{\tilde{\Phi}}|^2 \tag{8}$$

is performed where the sum is over all times at which data from a time series for Φ exist, and

$$\dot{\tilde{\Phi}} = \sum_\nu G_\nu(\mathbf{a}, \alpha_1, \cdots, \alpha_p)\mathbf{p}_\nu \tag{9}$$

is the tendency of the approximated state vector; $\mathbf{a}$ is determined by (5). Here it should be mentioned that, in contrast to the more general formulation of Hasselmann (1988), we have used the Euclidean metric for measuring errors throughout our work.

b. *Application to the B-model*

For an application of the PIP method to B-model data, the exact nature of the state vector has to be clarified. In our case state space is spanned by all spherical harmonic coefficients of τ and ψ that are possibly nonzero and for which the zonal wavenumber is nonnegative. In the case of an equatorially symmetric B-model, these are all coefficients with odd meridional wavenumbers. In the special case of baroclinic wave life cycles starting with a single normal mode at a given zonal wavenumber on a zonally symmetric wind, our state space is further reduced to coefficients describing the zonal wind, the wave, and all its upper harmonics in zonal wavenumber.

In order to make the following development more clear, we decompose the full state space into two subspaces. One of them comprises all zonally symmetric components forming a vector $\mathbf{z}$. The other contains all wave coefficients (zonal wavenumber $m \neq 0$). Its elements are denoted by a vector $\mathbf{w}$. Thus we can formally write

$$\Phi = \begin{pmatrix} \mathbf{z} \\ \mathbf{w} \end{pmatrix}. \tag{10}$$

For reasons of simplicity, each PIP is assumed to be an element of one of these two subspaces.

For the moment, simplifications of the zonally symmetric part are not sought so that we suppose that there are as many zonally symmetric PIPs as there are dimensions for them. They are taken to be the set of natural unit vectors of this space; that is, each of them corresponds to one zonal spherical harmonic coefficient of either ψ or τ; that is, they are defined by

$$\mathbf{p}_\nu = \begin{pmatrix} \mathbf{e}_\nu \\ \mathbf{0} \end{pmatrix}, \tag{11}$$

where $\mathbf{e}_\nu$ is the νth unit vector of the zonally symmetric subspace. Their coefficients are then given by

$$a_\nu = z_\nu. \tag{12}$$

The PIPs we are really looking for are the prominent ones existing in the wave subspace; that is,

$$\mathbf{p}_\nu = \begin{pmatrix} \mathbf{0} \\ \mathbf{q}_\nu \end{pmatrix}. \tag{13}$$

The evolution equations describing their development by interaction with each other and the zonal wind can be derived as follows: In appendix B it is shown that formally the tendencies for the elements of $\mathbf{z}$ and $\mathbf{w}$ can be written

$$\dot{z}_i = F_i + \sum_j A_{ij}z_j + \sum_{j,k} B_{ijk}w_j\overline{w_k} \tag{14}$$

$$\dot{w}_i = \sum_j C_{ij}w_j + \sum_{j,k} D_{ijk}z_jw_k + \sum_{j,k} (E_{ijk}w_jw_k + F_{ijk}w_j\overline{w_k}), \tag{15}$$

where F_i denotes all forcing contributions, A_{ij} dissipation and heating of the zonal wind, B_{ijk} wave mean zonal wind interaction, C_{ij} wave dissipation and the

beta-effect, D_{ijk} influences of the zonal wind on waves, and E_{ijk} and F_{ijk} nonlinear wave–wave interactions. Let us now assume that

$$\mathbf{w} = \sum_{\nu} a_\nu \mathbf{q}_\nu \tag{16}$$

holds exactly. Then by transformations that are completely analogous to the ones leading to (5), it can be shown that (14) and (15) can be replaced by

$$\dot{z}_i = \sum_j A_{ij}(z_j - Z_j) + \sum_{\nu,\mu} \alpha_{i\nu\mu} a_\nu \overline{a_\mu} \tag{17}$$

and

$$\dot{a}_\nu = \sum_\mu \omega_{\nu\mu} a_\mu + \sum_{j,\mu} \beta_{\nu\mu j} a_\mu z_j + \sum_{\mu,\rho} (\epsilon_{\nu\mu\rho} a_\mu a_\rho + \varphi_{\nu\mu\rho} a_\mu \overline{a_\rho}), \tag{18}$$

where

$$\alpha_{i\nu\mu} = \sum_{j,k} B_{ijk} q_{j\nu} \overline{q_{k\mu}} \tag{19}$$

$$\omega_{\nu\mu} = \sum_\kappa (T^{-1})_{\nu\kappa} \sum_{i,j} \overline{q_{i\kappa}} C_{ij} q_{j\mu} \tag{20}$$

$$\beta_{\nu\mu j} = \sum_\kappa (T^{-1})_{\nu\kappa} \sum_{i,k} \overline{q_{i\kappa}} D_{ijk} q_{k\mu} \tag{21}$$

$$\epsilon_{\nu\mu\rho} = \sum_\kappa \sum_{i,j,k} (T^{-1})_{\nu\kappa} \overline{q_{i\kappa}} E_{ijk} q_{j\mu} q_{k\rho} \tag{22}$$

$$\varphi_{\nu\mu\rho} = \sum_\kappa \sum_{i,j,k} (T^{-1})_{\nu\kappa} \overline{q_{i\kappa}} F_{ijk} q_{j\mu} \overline{q_{k\rho}}. \tag{23}$$

These tensor elements are the α_i connected to the PIP vectors $\mathbf{q}_\nu$ by boundary conditions. The elements of the matrix T are given by

$$T_{\nu\mu} = \sum_i \overline{q_{i\nu}} q_{i\mu}, \tag{24}$$

and the Z_j denote a forced stationary zonal solution such that

$$F_i + \sum_j A_{ij} Z_j = 0 \tag{25}$$

for all i. Thus the G_ν indeed have the form prescribed by (7), where the Z_i assume the role of the α_i not connected to the patterns by boundary conditions. Before applying this PIP model to multiple baroclinic wave life cycles in our two-layer model, let us briefly discuss how the method used for its derivation can be applied in connection with more general datasets.

c. *A PIP model for general datasets*

It can be shown that the method we used for obtaining a suitable PIP model can be generalized for analyses of most imaginable systems. For this, let us consider a general state space described by a state vector Φ. Possible examples could be data from a global circulation model or measured atmospheric data. It might be especially helpful not to consider the full state space but only a suitably chosen subspace, as for example, spectral coefficients of the streamfunction in two representative levels. We assume that for this subspace a model exists that describes the relevant dynamics at some accuracy. Keeping within the framework of the so far chosen example, this could be a quasigeostrophic two-layer model. The tendency equations of this model shall be given by

$$\dot{\Phi}_M = \mathbf{H}(\Phi, \alpha_1, \cdots, \alpha_q, t), \tag{26}$$

so that

$$\dot{\Phi} = \dot{\Phi}_M + \boldsymbol{\xi}, \tag{27}$$

with a not too large residual error $\boldsymbol{\xi}$. The parameters α_q denote external parameters as diabatic parameters, mean static stability, etc. For extracting from this a PIP model, we insert the expansion

$$\Phi = \sum_\nu a_\nu \mathbf{p}_\nu \tag{28}$$

into (26) and (27), combine the resulting equations under neglect of $\boldsymbol{\xi}$, perform the same transformations as in section (3.2), and arrive at

$$\dot{a}_\nu = G_\nu(\mathbf{a}, \alpha_1, \cdots, \alpha_q, t)|_p, \tag{29}$$

where

$$G_\nu(\mathbf{a}, \alpha_q, t)|_p = (N^{-1})_{\nu\mu} \sum_i \overline{p_{i\mu}} H_i(\sum_\nu a_\nu \mathbf{p}_\nu, \alpha_q, t) \tag{30}$$

and the index $\mathbf{p}$ indicates evaluation of the specified function using a given set of PIP vectors. The error function to be minimized is then given by

$$\epsilon(\alpha_1, \cdots, \alpha_q, \mathbf{p}_1, \cdots, \mathbf{p}_M, t) = \sum_t |\dot{\Phi} - \sum_\nu G_\nu(\mathbf{a}, \alpha_q, t)|_p \mathbf{p}_\nu|^2. \tag{31}$$

The a_ν are to be calculated via (5). If good knowledge about some external parameters exist, these might be kept fixed during the optimization. One great advantage of PIP analysis is, however, that all external parameters can also be determined by the optimization. One can thus hope to extract from rather complicated datasets elementary structures, together with their natural evolution equations, which describe most of the dynamics internal to the system. By analyzing these, a clearer picture of the essentials of this system might become available. In spite of the huge amount of numerical work certainly involved in practical development of such a PIP analysis, the prospects indicated could make it worthwhile. For the moment, however, let us come back to two-layer model data for a test whether such a projection can work at all.

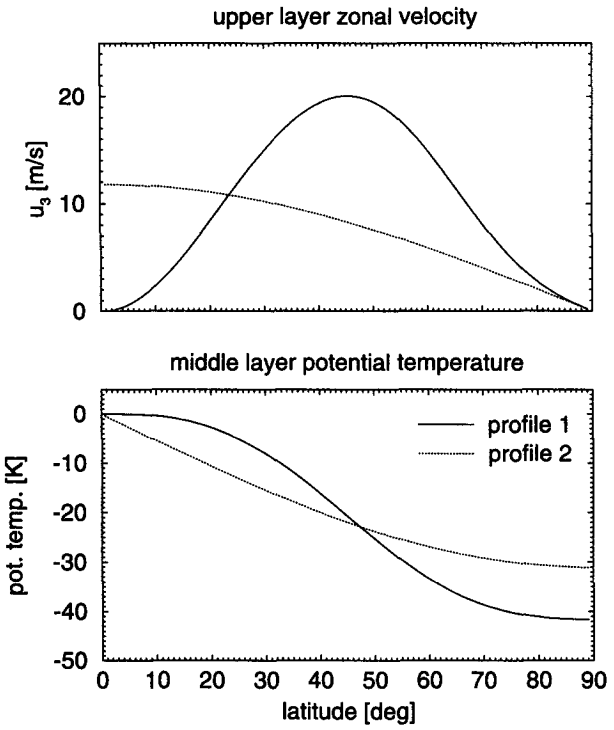

FIG. 1. The two zonal wind and potential temperature profiles used for initializing B-model integrations.

4. PIP analysis of multiple baroclinic wave life cycles

a. *The optimizations and their results*

In order not to detract from our main intention to test the possibilities of a PIP analysis, this paper only reports an analysis of the wave subspace spanned by the zonal wavenumber of the initial perturbation to the zonal wind, so that all upper harmonics are neglected. Then all wave–wave interaction terms (22)–(23) vanish, making the evolution equations especially simple. We will show that at least in the cases chosen here this approach is sufficient to extract the important wave PIPs dominating baroclinic wave life cycle behavior.

In a first experiment the values for surface friction and thermal damping are fairly typical ones: $h_N = 0.1$ d^{-1} and $k_s = 0.25$ d^{-1}. Two runs of 600 d with different initial conditions were made. In each of them the initial zonal mean surface velocity was zero. The upper-layer zonal mean velocity, however, was $u_3 \sim \sin^2 2\varphi$ in case 1 and $u_3 \sim \cos\varphi$ in case 2. The exact profiles with the resulting potential temperature distributions are shown in Fig. 1. In both cases forcing was chosen such that profile 1 is a stationary solution of the equations. As for the wave part of the initial conditions, time series 1 was initialized with a small contribution of the most unstable equatorially symmetric normal mode at $m = 6$ determined from an instability analysis of profile 1. The second most unstable normal mode for the same zonal wavenumber derived from this analysis was used for an initialization of time series 2.

For illustration, variation of the four Lorenzian energy types in case 1 relative to their initial values, the energy exchange coefficients and diabatic energy losses and gains are shown in Fig. 2 for the first 200 d. Normalization constants are $E_0 = (p_0\Omega^2 a_0^4)/g$ for energy and ΩE_0 for energy exchange, gain, or loss; p_0 is the surface pressure; g is the acceleration due to gravity; and K and A denote kinetic and available potential energy of the eddies (index E) or the zonal-mean wind (index Z). The diabatic terms are defined as follows: H_z denotes gains of A_z, H_E gains of A_E, D_E losses of K_E, and D_Z losses of K_Z due to surface drag, thermal damping, forcing, and horizontal diffusion. Multiple life cycles occur that have a clearly defined baroclinic growth phase where the waves mainly drain energy from A_Z. As documented by a rise in C_K (here conversion from K_E to K_Z, where C_A denotes conversion from A_Z to A_E and C_E from A_E to K_E), the decay phase has a barotropic contribution. It should, however, be noted that diabatic losses are comparable in magnitude to barotropic wave decay. As will be discussed later, the interplay of these two factors with each other seems to be responsible for the appearance of multiple life cycles. Since each time series contains about 20 life cycles, we consider our statistics to be reasonably good.

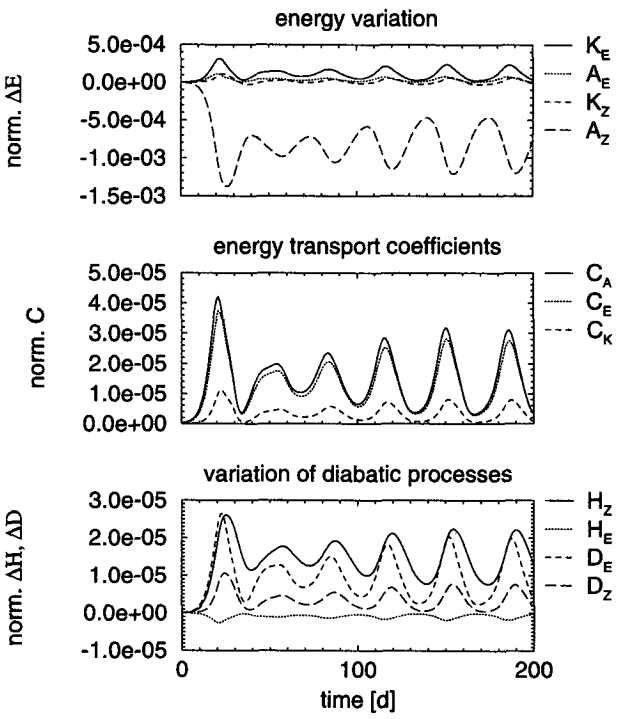

FIG. 2. Relative energy variation, energy exchange, and diabatic energy gains and losses for time series 1 with surface drag and thermal damping. Only the first 200 d are shown.

TABLE 1. Error of variances and tendency variances in a simulation of the two time series with thermal damping and surface friction with two or three PIPs.

	Time series 1		Time series 2	
	$\epsilon_1/10^{-4}$	$\epsilon_2/10^{-4}$	$\epsilon_1/10^{-4}$	$\epsilon_2/10^{-4}$
2 PIPs	24.4	17.8	25.7	6.18
3 PIPs	3.48	1.91	3.49	0.74

From each run we obtained a time series containing all spectral coefficients corresponding to $m = 0$ and $m = 6$ and the corresponding tendencies for every day. Time series 1 was then used to find the structures of a given number of wave PIPs by minimizing the error in explained tendency variance

$$\epsilon_1 = \frac{\epsilon}{\sum_t |\dot{\Phi}|^2}. \tag{32}$$

The minimization was performed numerically by applying a sequential quadratic programming algorithm as available in the NAG library (Ford and Pool 1984). The routine we used requires as input a subroutine calculating the error function and all its gradients at a specified point. The minimum is approached by a quasi-Newtonian search using an approximate Hessian matrix, which is estimated from the gradients of the error function at all points passed during the search. Zonal PIPs were kept fixed as defined in section 3. To get a second measure for the quality of the resulting patterns, these were also used to determine the error in explained variance

$$\epsilon_2 = \frac{\sum_t |\boldsymbol{\rho}|^2}{\sum_t |\Phi - \langle\Phi\rangle|^2} \tag{33}$$

of the time series. The brackets denote time averaging. The errors of explained tendency variance and variance of time series 2 were then calculated using the same patterns. Thus a measure of the generality of our results with respect to varying initial conditions could be obtained.

In the analysis, the wave subspace was first assumed to contain two PIPs. This number was then increased to three. Following the procedure described above, we found errors in explained tendency variance and variance as summarized in Table 1. It is found that explained variance and tendency variance do not depend very much on the time series that the PIPs are applied to. Note that the PIPs were determined by minimizing the tendency variance error of series 1. Thus it seems that the structures determined have a quite general nature and do not depend very much on the initial conditions of the examined time series. It should also be mentioned that the optimization result for the effectively forced stationary solution Z_j agrees nearly perfectly with profile 1 from Fig. 1. The method thus seems to be able to evaluate the forcing of a model from a time series of its spectral coefficients and their tendencies.

In order to demonstrate what the numbers in Table 1 mean we have projected the patterns derived onto the initial state of series 1 by applying (5). The result was used as the initial state for an integration of the PIP model tendency equations (17) and (18). The resulting time dependencies of the four energy types are compared with the analyzed data in Fig. 3. Two PIPs are only able to predict the first life cycle well, whereas the improvement gained by adding a third pattern is sufficient to capture most of the dynamics. The PIP model and the complete two-layer model produce very similar time dependencies for all energies. Minimum and maximum values as well as the length of the life cycles are reproduced. The PIP analysis therefore is able to extract from a model with good horizontal resolution few structures that describe most of the dynamics of multiple baroclinic wave life cycles in the model without having to perform a drastic truncation to, for example, R3 or R4. The identified patterns contain the full relevant R15 dynamics.

b. Discussion

The remaining question is what part the three PIPs play in the multiple life cycles. We will show how two of them describe the baroclinic growth phases, and the role of the remaining one in the decay phase will be discussed. In connection with this, the role of dissipation will also be considered. To show the ability of a PIP analysis to extract the basic dynamic signatures of a process, we will also point out some well-known features and show how they appear within the framework of a PIP model.

First of all it is useful to look a bit more closely at how much the PIPs contribute to the different phases of a life cycle. For this purpose we have projected the patterns onto day 150 of time series 1 and integrated the PIP model from there up to day 200. The dependence of amplitudes and phases of the coefficients a_ν of the three wave PIPs are displayed in Fig. 4. All three PIPs oscillate at only slightly varying frequencies. The corresponding periods are roughly between 6 and 8 days. PIP 1 and 2 are very similar to each other in the time dependence of their coefficients. PIP 3, on the other hand, is most active in the decay phase of a life cycle, whereas it does not contribute significantly to the growth phase. Further insight into the nature of the three PIPs can be gained by inspecting the latitude dependence of amplitude and phase of the patterns themselves (Fig. 5). The streamfunction maximum of PIP 1 is at midlatitudes, whereas for PIP 2 and 3 this is clearly shifted to lower or higher latitudes. The latter two are also more variable with respect to latitude.

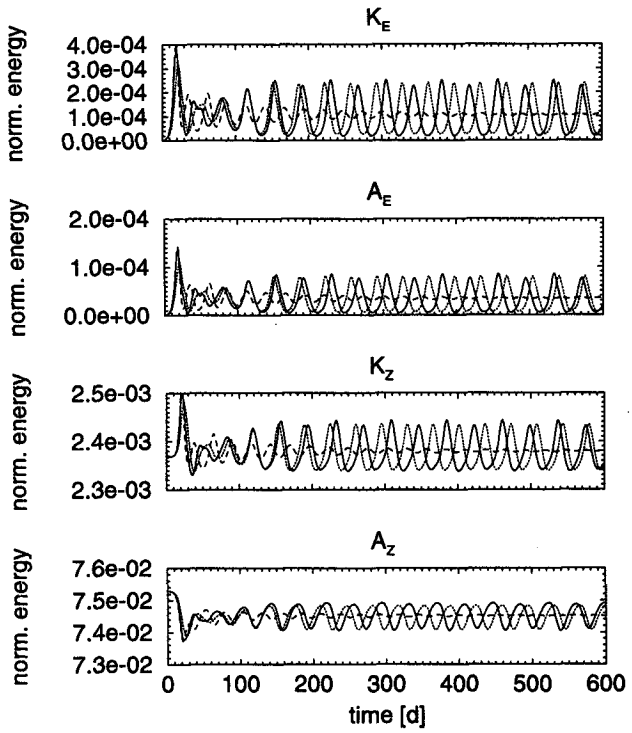

FIG. 3. Comparison of an integration of the PIP model for time series 1 with the real data (dotted line). Results of an the optimization using two wave PIPs are indicated by a dashed line, those from the three-PIP optimization by a solid line.

Higher meridional wavenumbers thus contribute to them more strongly than to PIP 1. There are also quite obvious differences in the phases of the streamfunction on the northern and southern flanks of the wind maximum. Most important is the inversion of the phase decay with latitude north of 60°N for PIP 3. Here northward momentum transport is replaced by southward transport. The same observations also hold at least qualitatively in the lower layer. Notable as a whole is the strong phase gradient of PIP 3, indicating a structure that is significantly tilted in the zonal direction so that effective momentum transport becomes possible. In both layers the phase difference of PIP 3 between 10° and 60°N is much larger than that of PIP 1.

From the above said, it should be expected that only PIP 1 and 2 are relevant for a simulation of the growth phases. To test this hypothesis we have projected the three patterns onto days representing the beginning of the early growth phase and days at the beginning of the late growth phase. The PIP model has then been integrated from there only considering PIP 1 or PIP 1 and PIP 2. It was found that the initial growth phase can be simulated well by using only PIP 1. It should therefore be the structure that bears the most similarity to the most unstable normal mode of profile 1. Indeed, the comparison of this normal mode with PIP 1 in Fig. 4 shows that this is the case. As for the late growth phase, it was found that it can be simulated by using PIP 1 and 2 but not PIP 1 only. By including PIP 2 only is the barotropic energy conversion C_K simulated appropriately. We thus conclude that PIP 2 captures the weakly nonlinear interaction with the zonal-mean zonal wind that increases in importance with increasing wave intensity.

However, projecting the patterns onto day 150 of the time series and integrating from there with and without PIP 3 shows that the latter is indispensable for an accurate description of the decay phase (Fig. 6): for some reason the eddy energies gain far too much. Due to the accordingly strong conversion processes, A_Z becomes too small, and K_Z gains too much. An equilibrium state is assumed, and no further life cycle results. Thus PIP 3 seems to be associated with some nonlinear interaction process that is not sufficiently contained in PIP 1 and 2.

In order to provide more insight into the dynamical nature of PIP 3, Fig. 7 shows the upper-layer meridional momentum and potential temperature transport and the corresponding Eliassen–Palm flux (EPF) divergence one would obtain if only one of the three PIPs were present. Momentum transport south of the jet maximum in the forced stationary solution is determined by PIP 2, whereas on the northern side PIP 3 has its maximum in momentum transport. At very high

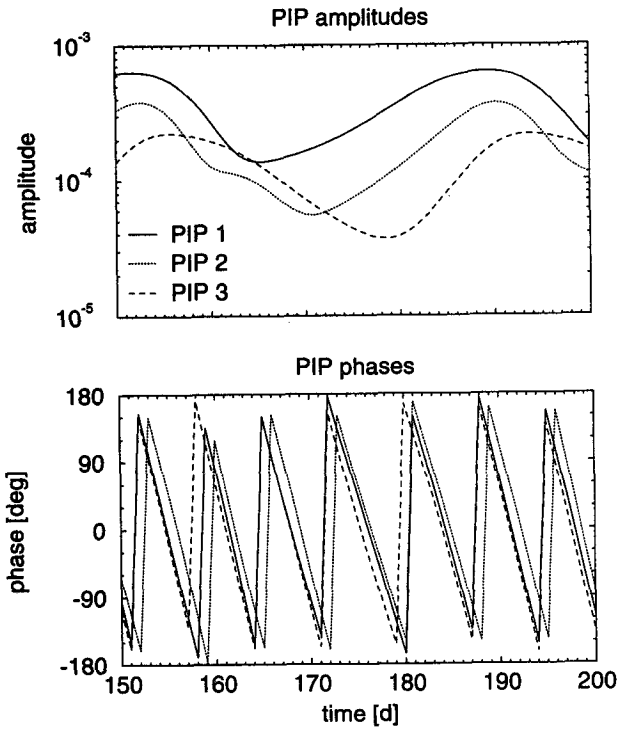

FIG. 4. Amplitudes and phases of the three wave PIPs corresponding to the three-PIP simulation of time series 1 between days 150 and 200. The patterns are numbered according to the maximum amplitudes they attain during a life cycle.

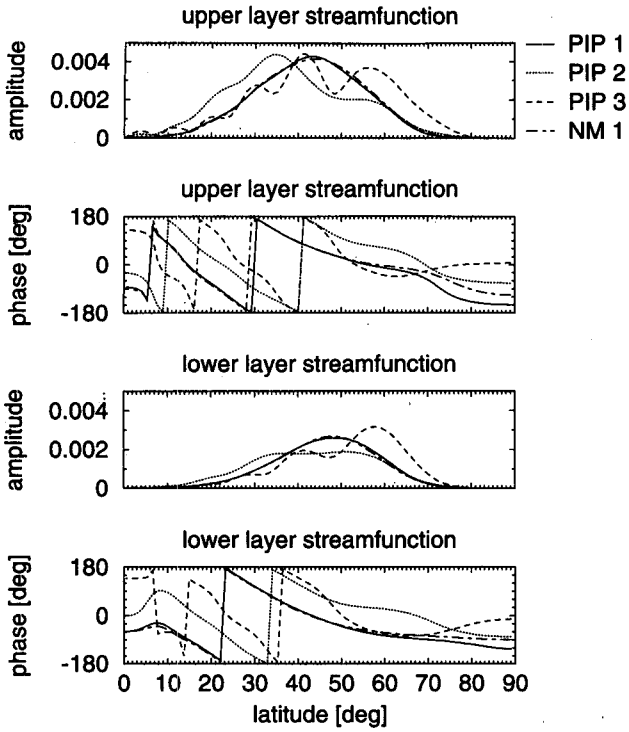

FIG. 5. Latitude dependence of the upper- and lower-layer streamfunction amplitudes and phases of the three wave PIPs corresponding to the three-PIP simulation of time series 1. The amplitudes are displayed in arbitrary units. The most unstable normal mode of the forced stationary state is also shown.

latitudes the latter also has a southward component. The resulting interaction with the zonally symmetric state is indicated by the EPF divergence. It is seen that PIPs 2 and 3 generate the barotropic structure of the jet on its flanks. The gradients are steepened. Thus barotropic wave decay is initiated, and higher wave number components are nonlinearly excited. This is reflected in the high wave number structure of the PIPs themselves, which is shown in Fig. 8 where the spectral intensity

$$I^m_{\nu n} = |\psi^m_{\nu n}|^2 + |\tau^m_{\nu n}|^2 \qquad (34)$$

is plotted versus the meridional wave number $n - m$. Here $\psi^m_{\nu n}$ and $\tau^m_{\nu n}$ denote the spectral components of the νth PIP in barotropic and baroclinic streamfunction (so far indicated by $q_{i\nu}$). In going from PIP 1 to PIPs 2 and 3 there is more energy at higher meridional wave numbers. We conclude that this pattern is necessary to describe a flux of potential enstrophy to higher latitudinal modes.

This is, however, only one part of the decisive properties of PIP 3. More information about this pattern can be gained by projecting PIPs 1–3 onto day 160 when PIP 3 is rather prominent and checking the energy conversion and diabatic losses with and without PIP 3. Thus the most important factors contributing to the wave decay, which is only possible in the presence of PIP 3, can be seen: PIP 3 increases C_E/C_A from 0.81 to 0.94, D_E/C_E from 0.60 to 0.93, and C_K/C_E from 0.23 to 0.34. By inclusion of PIP 3 only is it possible to describe the relative phases between the meridional wind field and the temperature and zonal wind field appropriately. The decay in K_E is due to two factors:

1) C_K increases simultaneously with PIP 3, and
2) especially in the later part of the decay phase, the relative contribution of dissipation of K_E is rather strongly enhanced.

Where does this dramatic change in the influence of dissipation originate? Closer inspection reveals that it is intimately connected with the high wave number structure of PIP 3. Assuming for the moment a wave streamfunction that contains only the νth PIP, it can be shown that D_E can formally be split up in contributions from thermal damping, surface friction, and horizontal diffusion in the following way:

$$D_E = |a_\nu|^2 [h_N \sum_{n=m}^{m+15} D_t(n-m) + k_s \sum_{n=m}^{m+15} D_s(n-m) + \kappa \sum_{n=m}^{m+15} D_h(n-m)]. \qquad (35)$$

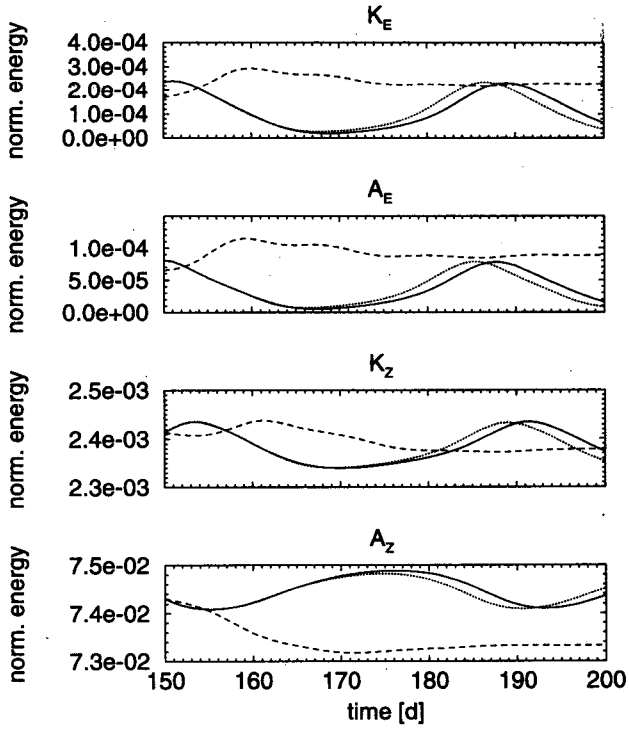

FIG. 6. Energy curves as derived from projecting only the two most prominent wave patterns (dashed line) or all wave patterns (solid) as derived from the three-PIP optimization of time series 1 on the numerical result for day 150 and integrating the PIP model from there up to day 200. Real data are indicated by a dotted line.

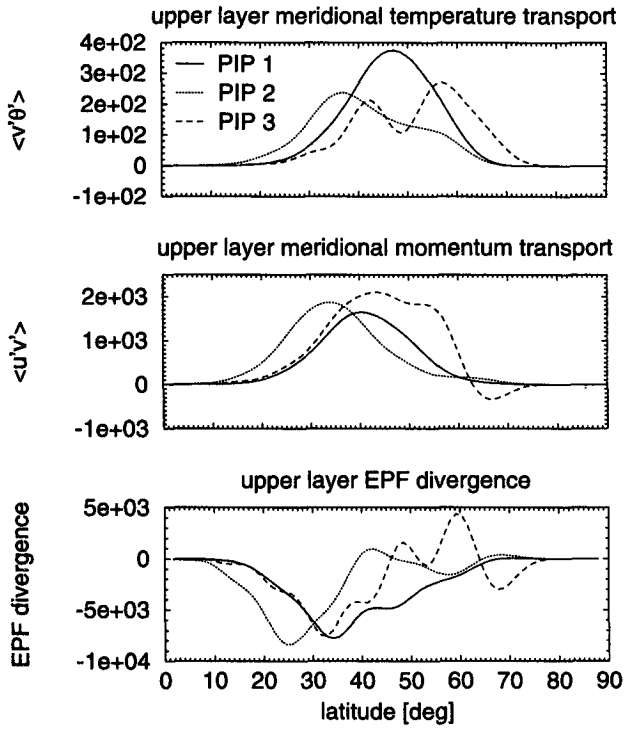

FIG. 7. Latitude dependence of the upper-layer meridional momentum transport, potential temperature transport, and upper-layer EPF divergence associable with each PIP in meaningless units.

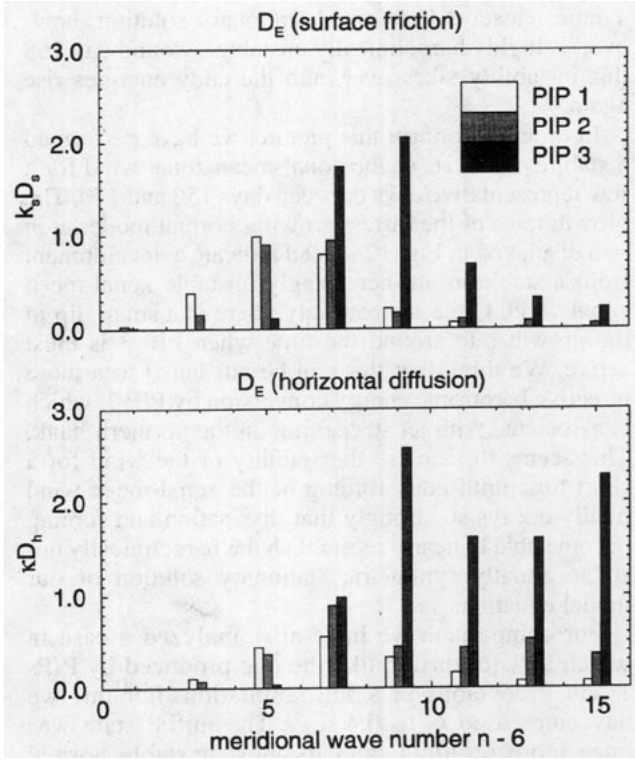

FIG. 9. Spectral composition of the eddy kinetic energy damping by surface friction and horizontal diffusion for all PIPs.

It turns out that the part resulting from thermal damping is virtually negligible for all patterns. The other two are displayed in Fig. 9. Due to contributions from higher wave numbers, PIP 3 is the most effectively dissipated. Therefore the enstrophy cascade to higher wave numbers that seems to be associated with this pattern also causes stronger eddy dissipation.

As a consequence of all these factors (including eddy dissipation), the eddy energies decay, and development of the zonally symmetric state now becomes increasingly dominated by the influences of surface friction, horizontal diffusion, and thermal forcing. Because wave activity decays so strongly it is much more able to reestablish the forced stationary solution than in the two-PIP case. Comparison of the development of the zonal-mean zonal wind in both cases shows that lower-layer winds are decelerated to lower values, and the upper-layer wind approaches the upper-layer profile

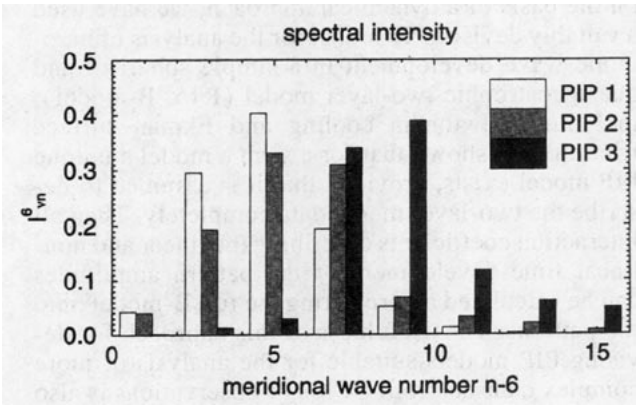

FIG. 8. Spectral intensity of the three identified PIPs.

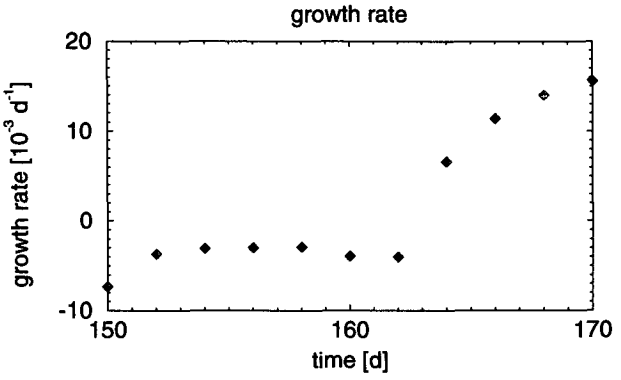

FIG. 10. Time dependence of the growth rate of the fastest-growing normal mode at $m = 6$ determined from a normal mode analysis of the zonally symmetric state in time series 1 between days 150 and 170.

1 more closely. The forced stationary solution, however, is highly baroclinically unstable. Around day 168 this instability takes over, and the eddy energies rise again.

In order to confirm this picture, we have performed a stability analysis of the zonal-mean zonal wind for a few representative days between days 150 and 170. The growth rates of the fastest growing normal modes at $m = 6$ displayed in Fig. 10 indeed indicate a development from a stable to an increasingly unstable zonal-mean zonal wind. Quite interestingly, there is a small dip in the growth rate around the time when PIP 3 is most active. We think that this can be attributed to a more effective barotropic energy conversion by PIP 3, which is associated with jet steepening on the northern flank. This seems to increase the stability of the wind for a short time until eddy forcing of the zonal-mean wind finally decays so strongly that dissipation and forcing become able to nearly reestablish the baroclinically unstable zonally symmetric stationary solution of our model equations.

For comparison we have also analyzed a case in which an equilibrium like the one produced by PIPs 1 and 2 develops in a full simulation. For this we have increased k_s to 0.4 d^{-1}. The initial state was once more profile 1, and its most unstable normal mode at $m = 6$. The corresponding two- and three-PIP simulations are shown in Fig. 11. As for the main qualitative features, two PIPs are now sufficient for a good simulation. They and the three from the three-PIP optimization are not shown here for conciseness. They look very similar to the ones of the less strongly damped case. It turns out that the third PIP resembling PIP 3 is not essential for explaining the late stationary phase. Projecting the three patterns onto day 100 of our time series, it is found that PIP 3 increases C_E/C_A from 0.83 to 0.85, D_E/C_E from 0.73 to 0.77, and C_K/C_E from 0.21 to 0.23. It therefore has a much weaker influence on eddy dissipation and barotropic energy conversion so that the eddy energies need not decay. The reason for this could be more effective damping of this structure due to the stronger surface friction. Checking the amplitude development, we have indeed found that it never attains an amplitude comparable to that of the most prominent PIP resembling PIP 1. To get a clearer picture of the late equilibrium we have also performed a stability analysis of the zonally symmetric state at day 100 of the full simulation. The corresponding growth rate is 8.5×10^{-4} d^{-1}. This fits into our interpretation of the equilibrium well. The jet has to be slightly unstable to facilitate some energy flux into the waves so that they do not decay because of dissipation. On the other hand the growth rate is smaller than in a growth phase of the less strongly damped case examined above so that wave intensity remains stable. To test whether the approximate equilibrium is due more to the barotropic governor mechanism (James

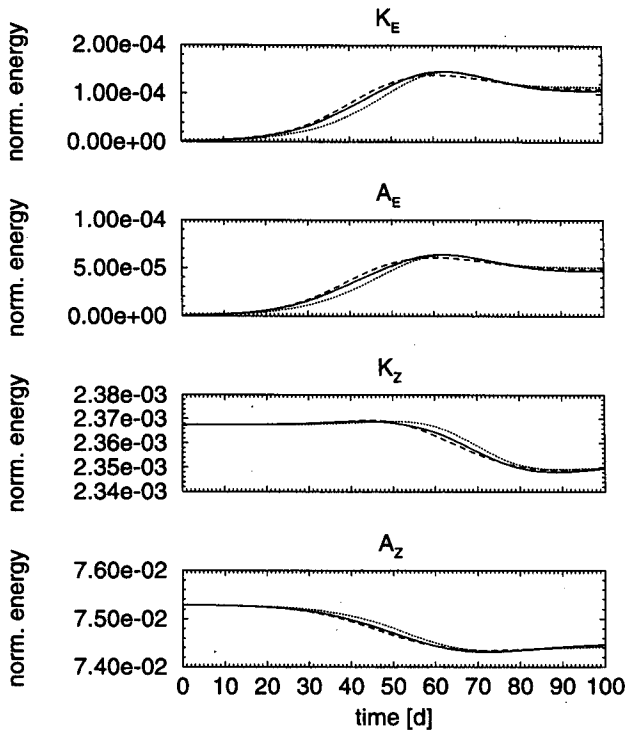

FIG. 11. Same as Fig. 3 but now with $k_s = 0.4$ d^{-1}.

1987) or baroclinic shear adjustment (Stone 1978), we have repeated the same stability analysis, now however replacing either the barotropic streamfunction or the baroclinic streamfunction of the zonal mean by the corresponding initial value at day 0. In the first case we find a maximal growth rate of 1.7×10^{-2} d^{-1}, in the second case it is -5.1×10^{-3} d^{-1}. From these values we conclude that it is more the increase of the barotropic wind component that makes the zonal-mean wind nearly stable.

5. Summary and conclusions

As a first step toward finding basic structures and processes underlying life cycles of baroclinic waves on the basis of a dynamical approach, we have used a suitably devised PIP model for the analysis of baroclinic wave development in a simple spherical and quasigeostrophic two-layer model (R15, B-model), including Newtonian cooling and Ekman surface friction. It is shown that for a such a model a unique PIP model exists, provided that it is assumed to describe the two-layer model data completely. Then all interaction coefficients describing the linear and nonlinear time development of the pattern amplitudes can be calculated by projecting the full B-model onto the patterns. The usefulness of this approach for devising PIP models suitable for the analysis of more complex datasets from GCMs or observations is also demonstrated.

For the moment we have concentrated on two-layer baroclinic wave life cycles with surface drag and thermal damping. Three PIPs are detected for typical values of these parameters that are able to describe the multiple life cycles sufficiently well both with respect to the minimum and maximum energies attained and to the length of the life cycles. PIPs found for one set of initial conditions are able to also explain time series with different initial conditions nearly equally well. Thus it can be assumed that they have a quite general nature. Only the interplay of forcing and dissipation with the nonlinear enstrophy cascade seems to have an influence on the decisive patterns that quickly develop irrespectively of the special initial conditions and dominate the model climate from then on.

Analyzing the interplay of the identified patterns with each other and the zonal-mean zonal wind, it is found that the most prominent PIP (PIP 1) is associated with the linear baroclinic growth phase. The second one (PIP 2) is necessary for a correct description of the weakly nonlinear interaction with the zonally symmetric state during the later part of this phase. PIPs 1 and 2 together are sufficient for an appropriate modeling of the whole growth phase.

The decay phase of a life cycle, however, cannot be captured by PIPs 1 and 2 alone. They are also not able to simulate the initialization of another life cycle after a decay phase. For this the last PIP (PIP 3) has to be taken into account. This one is associated with comparatively weak baroclinic conversion processes but stronger barotropic energy conversion. Its high-modal structure indicates that it is connected with a nonlinear transfer of potential enstrophy to higher wave numbers. In connection with this, it should also be noted that PIP 3 fits into the results of an analysis of quasigeostrophic turbulence in the presence of barotropic shear given by Sheperd (1987), where he has shown that the enstrophy cascade occurs by wave tilting into the zonal direction, which is compatible with the strong tilt of PIP 3. As a consequence of its high-modal structure, it is also strongly susceptible to dissipative damping. Due to this and energy transfer between K_E and K_Z, potential temperature and momentum transport by the waves are always at a level enabling thermal forcing and dissipation to act on the zonal flow such that a zonal-mean state can be reestablished that is rather similar to the forced stationary state. This is sufficiently baroclinically unstable so that a new life cycle can begin.

For a preliminary evaluation of the potential usefulness of PIP analysis one should be aware of Reinhold's (1986) ideas about structural organization of baroclinic waves in the presence of forcing and dissipation. From our investigations it appears that structural organization is not limited to as highly truncated models, as the one he has examined analytically. Reinhold predicts an increase of the degree of structural organization with increasing dissipation. Indeed, we also find that for increased dissipation the number of dynamically relevant patterns decreases. Moreover, in an additional analysis of the adiabatic case (initial conditions profile 1 and its most unstable normal mode at $m = 6$, for conciseness not to be discussed here in any detail), we have identified 6–8 patterns needed for a reasonable simulation. For sufficiently dissipative systems, PIPs therefore bear some potential as a tool for gaining further insight into the internal dynamics.

As a final remark, it should be mentioned that the interpretations given here are certainly determined by our choice of the dissipative parameters. How the PIPs depend on these will have to be addressed in a future paper. Additionally, the patterns found could well be limited to the wave subspace of the zonal wave number of the initial normal mode. Thus, in spite of some interesting features that have appeared in our analysis, the case examined is the most simple imaginable. It can be expected that an analogous examination of datasets that exhibit a higher degree of nonlinearity, as for example in the case of interaction of baroclinic waves with stationary waves or with higher zonal modes, will reveal more interesting details. Consequently a corresponding extension of our analysis is presently under preparation.

Acknowledgments. We are grateful to F. Kwasniok and Dr. B. Reinhold for valuable discussions. The comments of three anonymous reviewers have greatly helped in increasing the completeness and clarity of the paper. This work was partially supported by the Bundesministerium für Forschung und Technologie (07KFT55A7).

APPENDIX A

Derivation of the Tendency Equations for a B-Model with Thermal Damping and Surface Drag

The starting point for the derivation are the quasigeostrophic two-layer model equations formulated by Lorenz (1960). Replacing static stability by a constant parameter and including zonally symmetric vorticity forcing, surface friction, thermal damping, and horizontal diffusion gives the following set:

$$\frac{\partial}{\partial t}\nabla^2\psi = -J(\psi, \nabla^2\psi + f) - J(\tau, \nabla^2\tau) + k_s\nabla^2(\tau - \psi) + F_\psi - \kappa\nabla^2[\nabla^2(\nabla^2\psi)] \quad \text{(A1)}$$

$$\frac{\partial}{\partial t}\nabla^2\tau = -J(\tau, \nabla^2\psi + f) - J(\psi, \nabla^2\tau) + \nabla\cdot f\nabla\chi - k_s(\tau - \psi) - \kappa\nabla^2[\nabla^2(\nabla^2\tau)] \quad \text{(A2)}$$

$$\frac{\partial\theta}{\partial t} + J(\psi, \theta) - \bar{\sigma}\nabla^2\chi = h_N(\theta - \theta_f) - \kappa\nabla^2(\nabla^2\theta) \quad \text{(A3)}$$

$$bc_p\nabla^2\theta = \nabla\cdot f\nabla\tau, \tag{A4}$$

where χ denotes the velocity potential, θ potential temperature, θ_f its forcing (zonally symmetric), and $f = 2\Omega\sin\varphi$ the Coriolis parameter. Replacing the Coriolis parameter by a constant value $f_0 = 2\Omega\sin\varphi_0$ in the thermal wind equation (A4) yields the relationship

$$\theta = \frac{f_0}{bc_p}\tau + C, \tag{A5}$$

where C is a constant. Without loss of generality we assume $C = 0$. Also replacing the Coriolis parameter in the third term of (A2) by f_0 and using (A5) offers a simple way of combining (A2) and (A3) by eliminating the velocity potential from these. Scaling all terms appropriately, we thus end up with (1) and (2), where $\tau_f = (bc_p\theta_f)/f_0$.

APPENDIX B

Spectral Form of the B-Model Tendency Equations

For finding the spectral form of the B-model evolution equations we use the expansions

$$\psi(\varphi,\lambda,t) = \sum_{m=0}^{\infty}\sum_{l=m}^{\infty}[\psi_n^m(t)Y_n^m(\varphi,\lambda) + \overline{\psi_n^m}(t)\overline{Y_n^m}(\varphi,\lambda)(1-\delta_{m0})] \tag{B1}$$

$$\tau(\varphi,\lambda,t) = \sum_{m=0}^{\infty}\sum_{l=m}^{\infty}[\tau_n^m(t)Y_n^m(\varphi,\lambda) + \overline{\tau_n^m}(t)\overline{Y_n^m}(\varphi,\lambda)(1-\delta_{m0})], \tag{B2}$$

where Y_n^m are the well-known spherical harmonics. A useful property of these is

$$\overline{Y_n^m} = (-1)^m Y_n^{-m}. \tag{B3}$$

To express (1) and (2) in terms of the thus defined expansion coefficients, we need the interaction integrals

$$c_{n,n_1,n_2}^{m,m_1,m_2} = \int_{4\pi} d\Omega\overline{Y_n^m}J(Y_{n_1}^{m_1}, Y_{n_2}^{m_2}), \tag{B4}$$

which obey the following rules (Silberman 1954):

$$c_{n,n_2,n_1}^{m,m_2,m_1} = -c_{n,n_1,n_2}^{m,m_1,m_2} \tag{B5}$$

$$c_{n,n_1,n_2}^{m,-m_1,m_2} = (-1)^{m_1}c_{n_2,n_1,n}^{m_2,m_1,m} \tag{B6}$$

$$c_{n,n_1,n_2}^{m,m_1,-m_2} = (-1)^{m_2}c_{n_1,n,n_2}^{m_1,m,m_2}. \tag{B7}$$

They are only nonzero if the resonance condition

$$m = m_1 + m_2 \tag{B8}$$

is satisfied. Inserting (B1) and (B2) into (1) and (2), projecting the result onto the respective spherical harmonics, and using (B3) and (B5)–(B8), one obtains tendency equations that are formally identical to (14) and (15):

$$\frac{d\psi_n^0}{dt} = \frac{(F_\psi)_n^0}{n(n+1)} + k_s(\tau_n^0 - \psi_n^0) - \kappa[n(n+1)]^2\psi_n^0 + \sum_{m=1}^{\infty}\sum_{n_1,n_2=m}^{\infty}\frac{n_1(n_1+1)-n_2(n_2+1)}{n(n+1)}c_{n_1,n,n_2}^{m,0,m}(\psi_{n_1}^m\overline{\psi_{n_2}^m} + \tau_{n_1}^m\overline{\tau_{n_2}^m}) \tag{B9}$$

$$\frac{d\tau_n^0}{dt} = \frac{h_N r^2(\tau_f)_n^0}{n(n+1)+r^2} - \frac{h_N r^2\tau_n^0 + n(n+1)k_s(\tau_n^0-\psi_n^0)}{n(n+1)+r^2} - \kappa[n(n+1)]^2\tau_n^0 + \sum_{m=1}^{\infty}\sum_{n_1,n_2=m}^{\infty}c_{n_1,n,n_2}^{m,0,m}\frac{n_1(n_1+1)-n_2(n_2+1)-r^2}{n(n+1)+r^2}\psi_{n_1}^m\overline{\tau_{n_2}^m} + \sum_{m=1}^{\infty}\sum_{n_1,n_2=m}^{\infty}c_{n_1,n,n_2}^{m,0,m}\frac{n_1(n_1+1)-n_2(n_2+1)+r^2}{n(n+1)+r^2}\tau_{n_1}^m\overline{\psi_{n_2}^m} \tag{B10}$$

$$\frac{d\psi_n^m}{dt} = \frac{2im - n(n+1)k_s}{n(n+1)}\psi_n^m + k_s\tau_n^m - \kappa[n(n+1)]^2\psi_n^m + \sum_{n_1=0}^{\infty}\sum_{n_2=m}^{\infty}\frac{n_1(n_1+1)-n_2(n_2+1)}{n(n+1)}c_{n,n_1,n_2}^{m,0,m}(\psi_{n_1}^0\psi_{n_2}^m + \tau_{n_1}^0\tau_{n_2}^m) - \sum_{m_1=1}^{\infty}\sum_{n_1=m_1}^{\infty}\sum_{m_2=1}^{\infty}\sum_{n_2=m_2}^{\infty}\frac{n_2(n_2+1)}{n(n+1)}c_{n,n_1,n_2}^{m,m_1,m_2}(\psi_{n_1}^{m_1}\psi_{n_2}^{m_2} + \tau_{n_1}^{m_1}\tau_{n_2}^{m_2}) + \sum_{m_1=1}^{\infty}\sum_{n_1=m_1}^{\infty}\sum_{m_2=1}^{\infty}\sum_{n_2=m_2}^{\infty}\frac{n_1(n_1+1)-n_2(n_2+1)}{n(n+1)}c_{n_1,n,n_2}^{m_1,m,m_2}(\psi_{n_1}^{m_1}\overline{\psi_{n_2}^{m_2}} + \tau_{n_1}^{m_1}\overline{\tau_{n_2}^{m_2}}) \tag{B11}$$

$$\frac{d\tau_n^m}{dt} = \frac{n(n+1)}{n(n+1)+r^2} k_s \psi_n^m + \frac{2im - h_N r^2 - n(n+1)k_s}{n(n+1)+r^2} \tau_n^m - \kappa[n(n+1)]^2 \tau_n^m$$
$$+ \sum_{n_1=0}^{\infty} \sum_{n_2=m}^{\infty} c_{n,n_1,n_2}^{m,0,m} \frac{n_1(n_1+1) - n_2(n_2+1) - r^2}{n(n+1)+r^2} \psi_{n_1}^0 \tau_{n_2}^m$$
$$+ \sum_{n_1=0}^{\infty} \sum_{n_2=m}^{\infty} c_{n,n_1,n_2}^{m,0,m} \frac{n_1(n_1+1) - n_2(n_2+1) + r^2}{n(n+1)+r^2} \tau_{n_1}^0 \psi_{n_2}^m$$
$$+ \sum_{m_1=1}^{\infty} \sum_{n_1=m_1}^{\infty} \sum_{m_2=1}^{\infty} \sum_{n_2=m_2}^{\infty} \frac{n_1(n_1+1) - n_2(n_2+1) - r^2}{n(n+1)+r^2} c_{n,n_1,n_2}^{m,m_1,m_2} \psi_{n_1}^{m_1} \tau_{n_2}^{m_2}$$
$$+ \sum_{m_1=1}^{\infty} \sum_{n_1=m_1}^{\infty} \sum_{m_2=1}^{\infty} \sum_{n_2=m_2}^{\infty} \frac{n_1(n_1+1) - n_2(n_2+1) - r^2}{n(n+1)+r^2} c_{n_1,n,n_2}^{m_1,m,m_2} \psi_{n_1}^{m_1} \overline{\tau_{n_2}^{m_2}}$$
$$+ \sum_{m_1=1}^{\infty} \sum_{n_1=m_1}^{\infty} \sum_{m_2=1}^{\infty} \sum_{n_2=m_2}^{\infty} \frac{n_1(n_1+1) - n_2(n_2+1) + r^2}{n(n+1)+r^2} c_{n_1,n,n_2}^{m_1,m,m_2} \tau_{n_1}^{m_1} \overline{\psi_{n_2}^{m_2}}. \quad \text{(B12)}$$

REFERENCES

Baines, P. G., and J. S. Frederiksen, 1978: Baroclinic instability on a sphere in two-layer models. *Quart. J. Roy. Meteor. Soc.*, **104,** 45–68.

Barnes, J. R., and R. E. Young, 1992: Nonlinear baroclinic instability on the sphere: Multiple life cycles with surface drag and thermal damping. *J. Atmos. Sci.*, **49,** 861–878.

Branscome, L. E., W. J. Gutowski Jr., and D. A. Stewart, 1989: Effect of surface fluxes on the nonlinear development of baroclinic waves. *J. Atmos. Sci.*, **46,** 460–475.

Chang, E. K. M., 1993: Downstream development of baroclinic waves as inferred from regression analysis. *J. Atmos. Sci.*, **50,** 2038–2053.

Charney, J. G., 1947: The dynamics of long waves in a baroclinic westerly current. *J. Meteor.*, **4,** 135–162.

Eady, E. T., 1949: Long waves and cyclone waves. *Tellus,* **1,** 33–52.

Feldstein, S. B., and I. M. Held, 1989: Barotropic decay of baroclinic waves in a two-layer beta-plane model. *J. Atmos. Sci.*, **46,** 3416–3430.

Ford, B., and J. C. T. Pool, 1984: The evolving NAG library service. *Sources and Development of Mathematical Software,* W. Cowell, Ed., Prentice Hall, 375–397.

Frederiksen, J. S., 1981: Growth and vacillation cycles of disturbances in Southern Hemisphere flows. *J. Atmos. Sci.*, **38,** 1360–1375.

Gall, R. L., 1976: Structural changes of growing baroclinic waves. *J. Atmos. Sci.*, **33,** 374–390.

Hasselmann, K., 1988: PIPs and POPs: The reduction of complex dynamical systems using principal interaction and oscillation patterns. *J. Geophys. Res.*, **93,** 11 015–11 021.

James, I. N., 1987: Suppression of baroclinic instability in horizontally sheared flows. *J. Atmos. Sci.*, **44,** 3710–3720.

Lee, S., and I. M. Held, 1993: Baroclinic wave packets in models and observations. *J. Atmos. Sci.*, **50,** 1413–1428.

Lorenz, E. N., 1960: Energy and numerical weather prediction. *Tellus,* **12,** 364–373.

Mak, M., 1985: Equilibration in nonlinear baroclinic instability. *J. Atmos. Sci.*, **42,** 2764–2782.

Orlanski, I., and E. K. M. Chang, 1993: Ageostrophic geopotential fluxes in downstream and upstream development of baroclinic waves. *J. Atmos. Sci.*, **50,** 212–225.

Pedlosky, J., 1970: Finite amplitude baroclinic waves. *J. Atmos. Sci.*, **27,** 15–30.

Randel, W. J., 1990: Coherent wave–zonal mean flow interactions in the troposphere. *J. Atmos. Sci.*, **47,** 439–456.

——, and J. L. Stanford, 1985a: An observational study of medium-scale wave dynamics in the Southern Hemisphere summer. Part I: Wave structure and energetics. *J. Atmos. Sci.*, **42,** 1172–1188.

——, and ——, 1985b: The observed life cycle of a baroclinic instability. *J. Atmos. Sci.*, **42,** 1364–1373.

Reinhold, B., 1986: Structural determinism of linear baroclinic waves and simple nonlinear equilibration. *J. Atmos. Sci.*, **43,** 1484–1504.

Schnur, R., G. Schmitz, N. Grieger, and H. von Storch, 1993: Normal modes of the atmosphere as estimated by principal oscillation patterns and derived from quasigeostrophic theory. *J. Atmos. Sci.*, **50,** 2386–2400.

Sheperd, T. G., 1987: Rossby waves and two-dimensional turbulence in a large-scale zonal jet. *J. Fluid Mech.*, **183,** 467–509.

Silberman, I., 1954: Planetary waves in the atmosphere. *J. Meteor.*, **11,** 27–34.

Simmons, A. J., and B. J. Hoskins, 1978: The life cycles of some nonlinear baroclinic waves. *J. Atmos. Sci.*, **35,** 414–432.

Stone, P. H., 1978: Baroclinic adjustment. *J. Atmos. Sci.*, **35,** 561–571.

Thorncroft, C. D., B. J. Hoskins, and M. E. McIntyre, 1993: Two paradigms of baroclinic-wave life-cycle behavior. *Quart. J. Roy. Meteor. Soc.*, **119,** 17–55.

Young, R. E., and H. Houben, 1989: Dynamics of planetary-scale baroclinic waves during Southern Hemisphere winter. *J. Atmos. Sci.*, **46,** 1365–1383.